Applied Mathematics & Information Sciences
An International Journal

http://dx.doi.org/10.18576/amis/130315

Numerical Modeling of Heat and Mass Transfer with a Single-Phase Flow in a Porous Cavity

Mohamed F. El-Amin[1,2,*], *Shereen Abdel-Naeem*[2] *and Nehma A. Ebrahiem*[2]

[1] College of Engineering, Effat University, Jeddah 21478, KSA
[2] Mathematics Department, Faculty of Science, Aswan University, Aswan 81528, Egypt

Received: 5 Sep. 2018, Revised: 12 Feb. 2019, Accepted: 22 Feb. 2019
Published online: 1 May 2019

Abstract: This work is intended to study the problem of heat and mass transfer with single-phase flow in a porous cavity. The model of this problem consists of the conservation laws of energy, momentum, and mass. The cavity boundaries are described by mixed Dirichlet-Neumann boundary conditions. The momentum equation which is represented by Darcy's law has been solved with the continuity equation to give the pressure implicitly, then the velocity of the field has been calculated explicitly. Therefore, both energy equation and concentration equations are solved implicitly. The multiscale time-splitting implicit method has been used to treat the temporal discretization of the system of governing equations. The Courant-Friedrichs-Lewy condition has been used to achieve the time step-size adaptation. Some results are represented in graphs such as temperature, concentration, pressure, velocity, local Nusselt number and local Sherwood number. Two numerical cases are considered for different boundary conditions.

Keywords: Porous cavity, heat transfer, mass transfer, porous media, numerical simulation, CFL, time splitting

1 Introduction

Porous media are solid bodies that contain void spaces (so-called pores) and consist of a portion of space occupied by heterogeneous or multiphase matter [1]. In the last few decades, heat transfer in porous media has played an important role in many of engineering applications. Heat transfer in porous media involves a wide range of industrial applications such as geophysical systems, heat exchangers, thermal insulation of buildings, chemical reactors, drying processes, nuclear waste disposal, petroleum resources, packed bed spheres, grain storage, etc. Several studies gave an excellent picture of research being carried out in porous media [2,3]. Saeid and Pop [4] proposed the effect of viscosity dissipation on natural convection in a porous cavity, and they found that the viscous dissipation parameter increases with the decrease of heat transfer rate at the hot surface. Sheremet and Pop [5] studied the steady laminar-mixed convection inside a lid-driven square cavity filled with water-based nanofluid, and they found that the governing parameters have a greater effect on the heat transfer characters and the flow. Chalambaz et al. [6] studied the heat and mass transfer in a square porous cavity with differential temperature and concentration at the side walls, and they found that the heat transfer of the mixture and the mass transfer of the other phase can be maximized for specific values of the Lewis number of one phase. Carvalho and de Lemos [7] have presented the laminar free convection within a square porous cavity filled with a saturated fluid, and they found that the overall Nusselt number decreases rather than increases by increasing the void space within the porous material. The problem of free convection in a square porous cavity using a thermal nonequilibrium model had been invistegated by Baytas and Pop [8].

Implicit-Explicit (IMEX) method generally treats the linear terms implicitly and evaluates the others explicitly [9] to solve the differential equations that arise after discretization of time-dependent partial differential equations, the Implicit-Explicit technique has been improved several times [10]. Lang and Hundsdorfer [11] have studied systems of ordinary differential equations with both non-stiff and stiff parts included in the source term by a new class of Implicit-Explicit (IMEX) two-step methods of peer type. Burger et al. [12] proposed numerical schemes for the nonlinear equilibrium dispersive model for chromatographic processes with adsorption isotherms of Langmuir type which is treated

* Corresponding author e-mail: mohamed.elamin.kaust@gmail.com

by implicit diffusion and explicit convection. Kadalbajoo et al. [13] solved the partial integrodifferential equation that describes the nature of the option price under jump-diffusion model by using a radial basis function-based implicit-explicit numerical method.

The multiscale time-splitting methods have been considered in many numerical studies. Gravouil and Combescure [14] have introduced non-linear structural dynamics by the implicit-explicit multi-time-stepping method. A sub-time stepping method was described for computational fluid dynamics problems that utilize implicit-type time marching procedures to resolve transients, this was proposed by Bhallaudi et al. [15]. El-Amin et al. [16] presented an adaptive time-splitting scheme to investigate the problem of two-phase flow in heterogeneous porous media. The pressure and saturation equations are coupled by the capillary pressure which is linearized in terms of saturation. Zhang and Qian [17] have introduced the time viscosity-splitting method used for the Boussinesq problem. Caliari and Zuccher [18] proposed a numerical accurate algorithm of the well-known time-splitting Fourier spectral method for approximation of singular solutions of the Gross-Pitaevskii equation. El-Amin et al. [19] used multiscale time-splitting strategy to manage different time-step sizes for different physics. El-Amin et al. [20] have developed an iterative implicit scheme for nanoparticles transport with two-phase flow in porous media. Multiscale adaptive time-splitting technique for nonisothermal two-phase flow and nanoparticles transport in a heterogeneous porous medium have been investigated [21].

In this paper, we introduce a multiscale adaptive time-splitting scheme to simulate the problem of heat and mass transfer with a single-phase flow in a porous cavity. An IMEX algorithm has been used such that the equations of pressure, temperature and concentration have been treated implicitly in a consequence way. Also, the Cell-Centered Finite Difference (CCFD) method has been used for the spatial discretization. On the other hand, the Courant-Friedrichs-Lewy (CFL) stability condition has been used to adapt the proposed scheme by dividing time-steps as needed. Selected results of two cases of different boundary conditions are considered. Contours of the temperature, the concentration, the pressure, and the velocity, as well as the local Nusselt number and the Sherwood number are represented in graphs.

2 Mathematical Modeling

This mathematical model describes the basic equations of non-isothermal single-phase flow in porous media governed by the conservation laws of momentum, energy, and mass; in terms of pressure, temperature and concentration. We consider two distinct numerical cases in the porous cavity based on boundary conditions types.

The energy conservation equation in porous media can be represented as [21],

$$\frac{\partial}{\partial t}\left[(1-\phi)\rho_s c_{p,s}+\phi\rho c_p)T\right]+\rho\mathbf{u}\cdot\nabla T=\nabla\cdot\left[(1-\phi)h_s+\phi h\right]\nabla T+\rho Q_t \tag{1}$$

Momentum conservation in porous media is represented in the form of Darcy's law [22],

$$\mathbf{u}=-\frac{K}{\mu}\left(\nabla p+g\rho_0\left[1-\beta(T-T_r)-\beta^*(c-c_0)\right]\nabla z\right) \tag{2}$$

In the Boussinesq approximation, the density of the body force term is calculated by,

$$\rho=\rho_0\left[1-\beta(T-T_r)-\beta^*(C-C_0)\right],$$

$$\beta=-\frac{1}{\rho_0}\frac{\partial\rho_\alpha}{\partial T},$$

and

$$\beta^*=-\frac{1}{\rho_0}\frac{\partial\rho_\alpha}{\partial C}.$$

Mass conservation equation is represented by,

$$\nabla\cdot\mathbf{u}=q \tag{3}$$

where ϕ is the porosity, ρ_s is the density of the solid phase, c_p [J/Kg.K] is the heat capacity, T[K] is the temperature and h [J/K.m.s] is the thermal conductivity. $\mathbf{u}$ and ρ are, respectively, velocity and density, Q_t is the heat source term. K is the permeability. g is the gravitation acceleration, and z is the depth. p, and μ are, respectively, pressure, and viscosity. The temperature difference may cause a convective flow, which is represented by the Boussinesq approximation in the body force term of Eq. (2). β is the thermal expansion coefficient, β^* is the solute expansion, C is the concentration, C_0 is the initial concentration, T_r is a temperature reference and q is the external mass flow rate.

Substituting by (2) into (3), then the pressure equation can be rewritten as,

$$-\nabla\cdot\frac{K}{\mu}\left(\nabla p+g\rho_0\left[1-\beta(T-T_r)-\beta^*(C-C_0)\right]\nabla z\right)=q \tag{4}$$

Concentration equation (mass transport) in the water phase may be represented as [39],

$$\phi\frac{\partial C}{\partial t}+\nabla\cdot(\mathbf{u}C-D\nabla C)=Q_c \tag{5}$$

where Q_c is the rate of change of particle volume belonging to a source/sink term. The diffusion-dispersion tensor is defined by,

$$D=Q\tau D_t,\quad D_t=D^{Br}+D^{disp} \tag{6}$$

where τ is the tortuosity parameter of the water phase. Br is the Brownian diffusion and D^{disp} is the dispersion coefficient which is defined by [23],

$$Q\tau D^{disp} = d_t|\mathbf{u}|\mathbf{I} + (d_l - d_t)(\mathbf{u}\mathbf{u}^t)/|\mathbf{u}| \tag{7}$$

Thus,

$$D = (Q\tau D^{Br} + d_t|\mathbf{u}|)\mathbf{I} + (d_l - d_t)(\mathbf{u}\mathbf{u}^t)/|\mathbf{u}| \tag{8}$$

where d_l and d_t are, respectively, the longitudinal and transverse dispersion coefficients.

The local surface heat fluxes, q_x, and q_y are defined as,

$$q_x = -k\frac{\partial T}{\partial x}|_{x=0}, \tag{9}$$

$$q_y = -k\frac{\partial T}{\partial y}|_{y=0}. \tag{10}$$

where k is the effective thermal conductivity of the fluid. The local Nusselt number measures the competition between convection and conduction heat flows, defined by,

$$Nu_x = \frac{q_x L_x}{(T_w - T_0)k} = -\frac{L_x}{(T_w - T_0)}\frac{\partial T}{\partial x}|_{x=0} \tag{11}$$

$$Nu_y = \frac{q_y L_y}{(T_w - T_0)k} = -\frac{L_y}{(T_w - T_0)}\frac{\partial T}{\partial y}|_{y=0} \tag{12}$$

where L_x, L_y are the characteristic lengths. Similarly, the local surface mass fluxes, j_x, j_y may be defined as,

$$j_x = -D\frac{\partial C}{\partial x}|_{x=0} \tag{13}$$

$$j_y = -D\frac{\partial C}{\partial y}|_{y=0} \tag{14}$$

Therefore, the local Sherwood number which represents the ratio of the convective mass transfer to the rate of diffusive mass transport is given by,

$$Sh_x = \frac{j_x L_x}{(C_w - C_0)D} = -\frac{L_x}{(C_w - C_0)}\frac{\partial c}{\partial x}|_{x=0} \tag{15}$$

$$Sh_y = \frac{j_y L_y}{(C_w - C_0)D} = -\frac{L_y}{(C_w - C_0)}\frac{\partial C}{\partial y}|_{y=0} \tag{16}$$

3 Numerical Method

The time-splitting technique subdivides an equation including several physical processes into a number of simpler equations, and instead of applying the one-dimensional advection-diffusion equation over one time step, it may be splitting into the pure advection equation and the pure diffusion equation each to be applied over half a time step and it solves the simpler diffusion and advection equations [24]. A numerical strategy for time discretization has been presented [25]. In this model, the pressure time-step size can be taken larger than the dependent variables such as temperature. For pressure, the total time interval, [0, T], is divided into N_p , time-steps, namely, $0 = t_0 < t_1 < ... < t_{N_p=T}$, with a time step of length, $\Delta t^k = t^{k+1} - t^k$. The subscript $k+1$ represents the current time step and the subscript k represents the previous time step. For temperature and concentration, each interval, (t^k, t^{k+1}), is divided into $N_{p,c}$ subintervals, i.e. $(t^k, t^{k+1}) = \cup_{l=0}^{N_{p,c}}(t^{k,l}, t^{k,l+1})$. In our study, we assume the temperature and concentration have the same discretization level, and we use backward Euler time discretization for the time derivative of equations of temperature and concentrations. Hence the pressure equation becomes,

$$-\nabla\cdot\frac{K}{\mu}\left(\nabla p^{k+1} + g\rho_0\left[1 - \beta(T^k - T_r) - \beta^*(C^k - C_0)\right]\nabla z\right) = q^{k+1} \tag{17}$$

The energy equation and concentration equation are computed implicitly as,

$$\left[(1-\phi)\rho_s c_{p,s} + \phi\rho(T^k)c_p)\right]\frac{T^{k,l+1} - T^{k,l}}{\Delta t} + \rho^k\mathbf{u}^{\mathbf{k+1}}\cdot\nabla T^{k,l+1} = \nabla\cdot\left[(1-\phi)h_s + \phi h\right]\nabla T^{k,l+1} + \rho Q_t^{k,l+1} \tag{18}$$

$$\phi\frac{C^{k,l+1} - C^{k,l}}{\Delta t} + \nabla\cdot(\mathbf{u}^{k+1}C^{k,l+1} - D\nabla C^{k,l}) = Q_c^{k,l+1} \tag{19}$$

Hence, we update the porosity, the permeability, and the density.

The Courant-Friedrichs-Lewy (CFL) condition has been used to ensure that CFL$<$ 1. The CFLs for the temperature equations are,

$$\mathrm{CFL}_{T,x} = \frac{u_x\Delta t^{k,l}}{\Delta x} \tag{20}$$

$$\mathrm{CFL}_{T,y} = \frac{u_y\Delta t^{k,l}}{\Delta y} \tag{21}$$

and for the concentration equation are given by,

$$\mathrm{CFL}_{C,x} = \frac{u_x\Delta t^{k,l}}{\Delta x} \tag{22}$$

$$\mathrm{CFL}_{C,y} = \frac{u_y\Delta t^{k,l}}{\Delta y} \tag{23}$$

In this algorithm, the initial time step of the temperature and concentration equations is taken as the pressure time step, i.e., $\Delta t^{k,0} = \Delta t^k$. Then, we check if $\mathrm{CFL}_{C,x} > 1$ or $\mathrm{CFL}_{C,y} > 1$, the concentration time step will be divided into smaller steps, then, $\mathrm{CFL}_{C,x}$ and $\mathrm{CFL}_{C,y}$ will be recalculated and so on until we get $\mathrm{CFL}_{C,x} < 1$ and $\mathrm{CFL}_{C,y} < 1$. Similarly, $\mathrm{CFL}_{T,x}$ and $\mathrm{CFL}_{T,y}$ can be used as $\mathrm{CFL}_{C,x}$ and $\mathrm{CFL}_{C,y}$.

Table 1: Physical parameters of the model

Parameter	Value	Unit
T_0	300	K
T_w	360	K
C_0	0	–
C_w	1	–
p_0	1.0E6	N/m^2
u_{in}	0.03	m/year
ϕ	0.3	–
c_p	800	J/Kg. K
ρ_s	2550	kg/m^3
μ	1.0E-03	Pa s
p_0	1.0E6	Pa
ρ_s	2500	kg/m^3
ρ_w	1000	kg/m^3
D	1E-5	m^2/s
h_s	0.718	$W/(m/K)$
h_w	0.6	$W/(m/K)$
β_w	0.001	K^{-1}
β_w	0.001	K^{-1}
g	9.8	m/s^2
md	9.86923E-16	m^2

4 Results and Discussion

The governing equations have been solved numerically using the numerical method which are explained above, with two different cases of the boundary conditions as shown in Fig. 1(a, b). The boundary conditions of each case are shown on the figure. In Case 1, all boundaries are described by Dirichlet boundary conditions except in the west boundary, no-flow boundary conditions with velocity inlet have been used. The physical parameters are shown in Table 1.

The domain is a square with a 1×1 m and which is uniformly discretized into 50×150 rectangle cells. We use the outer time loop k for the number of steps, then, the time-step sizes, Δt^l and Δt^m which are explained later are calculated based on the CFLs. In order to investigate the accuracy of the current numerical scheme, Table 2 presents some error estimates for temperature and concentration for various values of the number of outer time steps k. It can be seen from Table 2 that the error decreases as the number of time steps increases. It is interesting to note that the temperature error is very small and approaches zero, however, the concentration error needs bigger time step numbers to reach the desired approximation.

Now, let us introduce the cases of study:

Case 1: All the walls of the square cavity are kept at a cool temperature T_c and concentration C_c except the center of the left wall is kept at a high temperature T_h and a high concentration C_h as shown in Fig. 1(a). The boundary conditions are described as follows:

$$x = 0, 0 \le y \le L, T = T_c, C = C_c, \frac{\partial p}{\partial x} = 0,$$

Table 2: Error estimates for various values of number of time steps k.

k	$\|T^{n+1,k+1} - T^{n+1,k}\|$	$\|C^{n+1,k+1} - C^{n+1,k}\|$
1000	3.2895E-12	0.0088
1500	3.0320E-12	0.0059
2000	2.6311E-12	0.0044
2000	2.6021E-12	0.0029

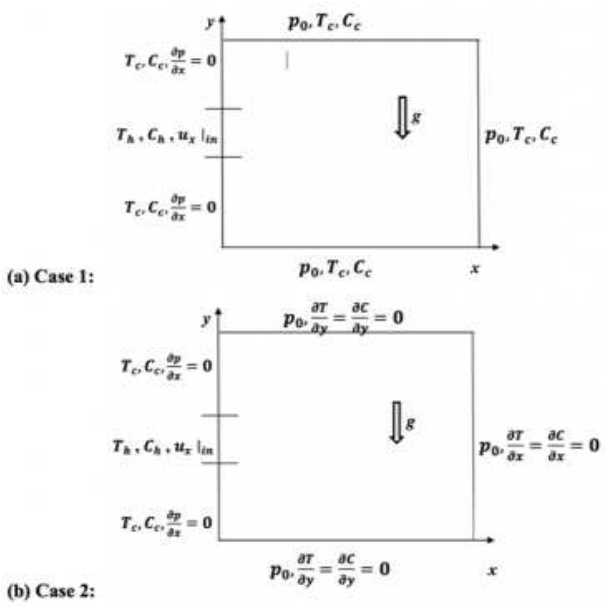

Fig. 1: Schematic diagram of the 2D square porous cavity (a) case 1, and (b) case 2.

$$T_{in} = T_h, C_{in} = C_h, u = u_{in},$$
$$0 \le x \le L, y = 0, T = T_c, C = C_c, p = p_0,$$
$$x = L, 0 \le y \le L, T = T_c, C = C_c, p = p_0,$$
$$0 \le x \le L, y = L, T = T_c, C = C_c, p = p_0$$

where *in* refers to the injection location (inlet), we consider the velocity on all cells to be zero (no-flow boundary conditions) except for the central cells being equal to 0.03 m/year. The inlet is located at the center (width is 0.3 m).

Case 2: All the walls of the square cavity are adiabatic and isothermal with constant Dirichlet pressure, except for the center of the left wall is kept at hot temperature T_h and high concentration C_h and the upper and lower of left wall are kept at cold temperature and low concentration with no-flow Neumann boundary condition as shown in Fig. 1(b). The boundary conditions are described as follows:

$$x = 0, 0 \le y \le L, T = T_c, C = C_c, \frac{\partial p}{\partial x} = 0,$$
$$T_{in} = T_h, C_{in} = C_h, u = u_{in},$$

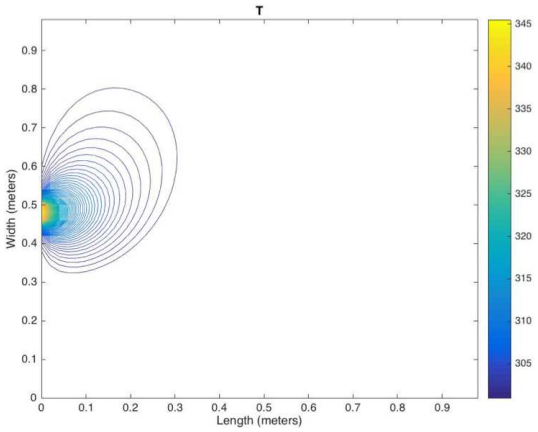

Fig. 2: Temperature distribution of case 1.

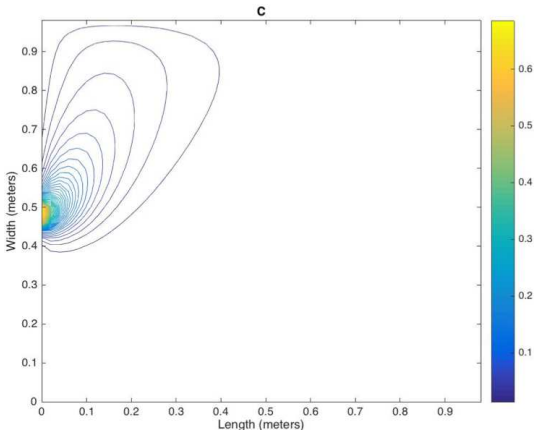

Fig. 3: Concentration distribution of case 1.

$$0 \le x \le L, y = 0, \frac{\partial T}{\partial y} = \frac{\partial C}{\partial y} = 0, p = p_0,$$

$$x = L, 0 \le y \le L, \frac{\partial T}{\partial x} = \frac{\partial C}{\partial x} = 0, p = p_0,$$

$$0 \le x \le L, y = L, \frac{\partial T}{\partial y} = \frac{\partial C}{\partial y} = 0, p = p_0$$

The results of the Case 1 have been presented in the following figures (Fig. 2 - Fig. 7). Fig. 2 shows the temperature distribution of case 1. The temperature in this figure is seen to be high at the inlet with a maximum value of $T_{max} = 340$ K and then decreases because the other walls are cooled. It is also interesting to observe the buoyancy effect on the temperature contours in Fig. 2. This appears for a small inlet velocity for which the buoyancy force dominates the advection force.

Concentration profiles in the square cavity of case 1 are plotted in Fig. 3. From this figure, we can see a reduction in the concentration everywhere but it is high at the inlet. The concentration decreases gradually from the inlet to the far-field location.

The pressure distribution of case 1 is shown in Fig. 4. From this figure, we can see that the pressure decreases gradually from the inlet area to the other points. The high pressure is due to the fluid injection from the center of the left wall. The velocity distribution of case 1 has been plotted in Fig. 5. The maximum value of velocity occurs along the central portion of the left wall and then decreases as it moves away from the inlet.

Fig. 6 illustrates the local Nusselt number profiles along the left wall, right wall, upper wall, and lower wall. It is clear from this figure that the higher local Nusselt number is located in the center of the left wall, which indicates that the heat transfer rate is high in the region. Moreover, it is interesting to notice that the shape of the local Nusselt number is symmetric and represented by a Gaussian distribution. From this figure, it can be seen that the heat transfer rate on the right wall is very high at the edges of the right wall and it increases from the bottom to

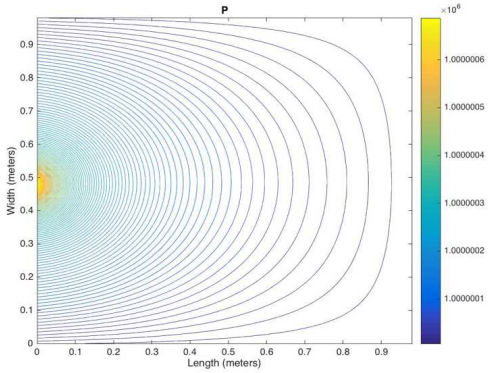

Fig. 4: Pressure distribution of case 1.

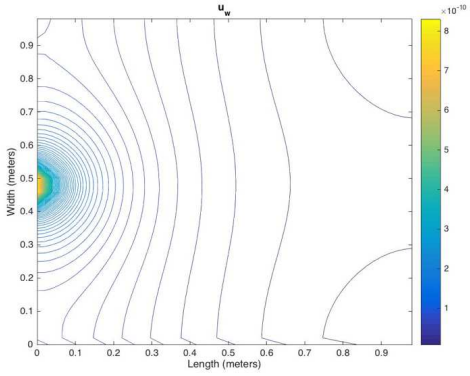

Fig. 5: Velocity distribution of case 1.

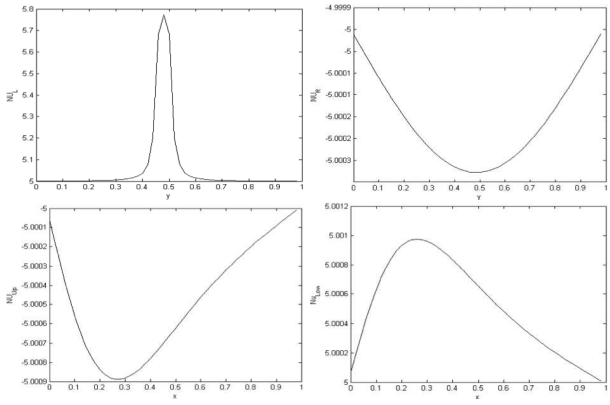

Fig. 6: Local Nusselt number distributions along the left wall, the right wall, the upper wall, and the lower wall

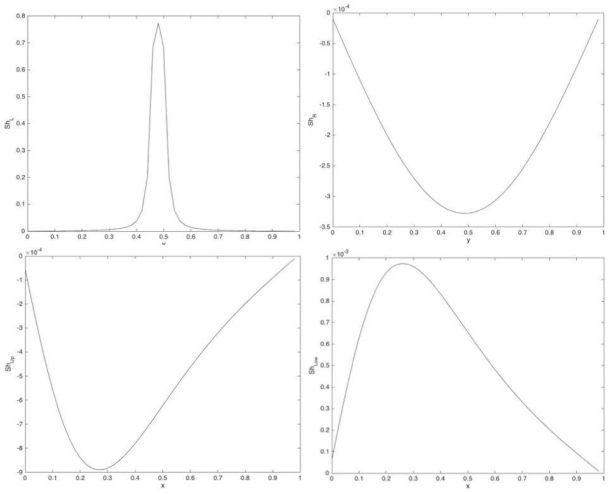

Fig. 7: Local Sherwood number distributions along the left wall, the right wall, the upper wall, and the lower wall

the top. The negative sign indicates that heat transfer direction is from the fluid to the solid wall. Also, the heat transfer rate at the upper wall is high at the top left portion and then decreases to the right portion. Also, this figure shows that the local Nusselt number at the lower wall is high at the left portion and then decreases to the right portion. This is a very small variation in Nu but it is not constant. This may indicate that the wall the field temperature adjacent to the wall is very close the wall temperature. Moreover, one may notice that the behavior of the heat transfer on the upper wall is quite similar to the behavior of the heat transfer on the lower wall but with opposite sign, i.e. heat flows in opposite directions.

Fig. 7 illustrates the local Sherwood number profiles along the left wall, the right wall, the upper wall, and the lower wall. It can be seen from this figure that the local Sherwood number profiles along the left wall and the right wall are symmetric around the center of the y-axis and it decreases gradually from the center to the upper to the lower corners. It can be seen that the mass transfer rate on the left wall is high at the inlet location of the right wall and it decreases from the bottom to the top. The negative sign indicates that mass transfer direction is from the fluid to the solid wall. Also, the mass transfer rate on the right wall is very small. The local Sherwood number on the upper wall and the left wall has a similar behavior and same order of magnitude with different signs. The local mass transfer rate has maximum values at $x \approx 0.1$.

The results of the Case 2 have been presented in the following figures (Fig. 8 -Fig. 11). The temperature distribution of case 2 are shown in Fig. 8. It can be seen from this figure that the temperature is high at and around the inlet location with a maximum value of T_{max}=340 K and then it decreases gradually faraway because the other walls are kept adiabatic with a constant pressure. This may be interpreted as the heat transfer changes from the mixed convection region to a is due to purely conduction region. On the other hand, the amount of heat which is

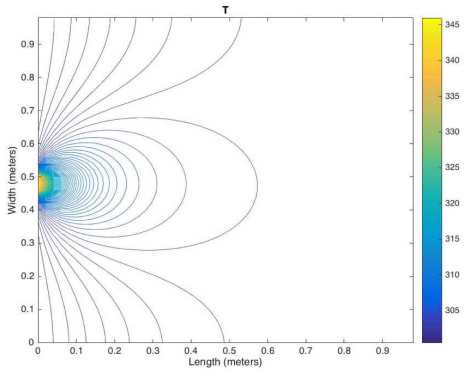

Fig. 8: Temperature distribution of case 2.

transferred to the lower wall and the upper wall, as a result of convection.

Fig. 9 shows the concentration distribution of case 2. The behavior of the concentration of this figure is similar to the temperature distribution in Fig. 8, which can be interpreted similarly with respected to mass transfer and solute convection. Fig. 10. shows the local Nusselt number at the left wall, the right wall, the upper wall, and the lower wall of Case 2. The local heat transfer at the left wall of the cavity is symmetric around the inlet area and its highest values located at the center of the left wall and decreases gradually to the lower to the upper parts. On the other hand, the heat transfer rate on the right wall of the cavity is very high at the center but with opposite direction, while, the negative sign indicates that heat transfer direction is from the fluid to the solid right wall. Also, the figure shows that the local Nusselt number at the upper wall increases close to the left wall and

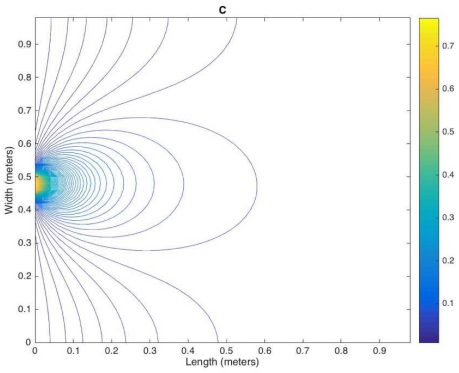

Fig. 9: Concentration distribution of case 2.

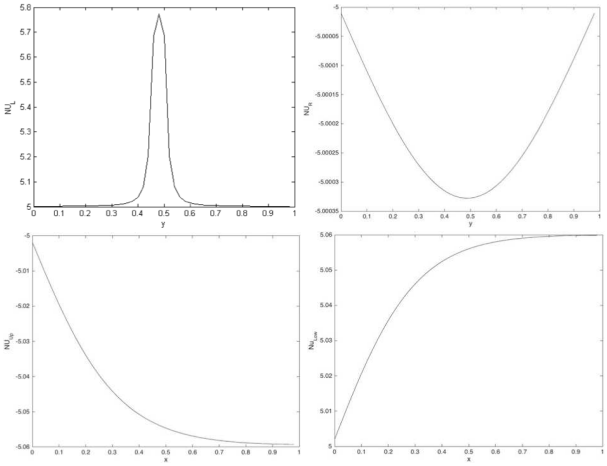

Fig. 10: Local Nusselt number distributions along the left wall, the right wall, the upper wall, and the lower wall, Case 2

decreases close to the right wall. The opposite is true for the local heat transfer on the lower wall of the cavity.

Fig. 11 shows the local Sherwood number profiles along the left wall, the right wall, the upper wall, and the lower wall. The local mass transfer in terms of local Sherwood number at the left wall of the cavity is symmetric around the inlet and behaves very similar to the Sherwood number at the left wall of Case 1. The mass transfer rate on the right wall of the cavity is very high at the center and decreases towards the left side and decreases more towards the right side. On the other hand, the local Sherwood number at the upper wall increases close to the left wall and decreases close to the right wall. The opposite is true for the local heat transfer on the lower wall of the cavity.

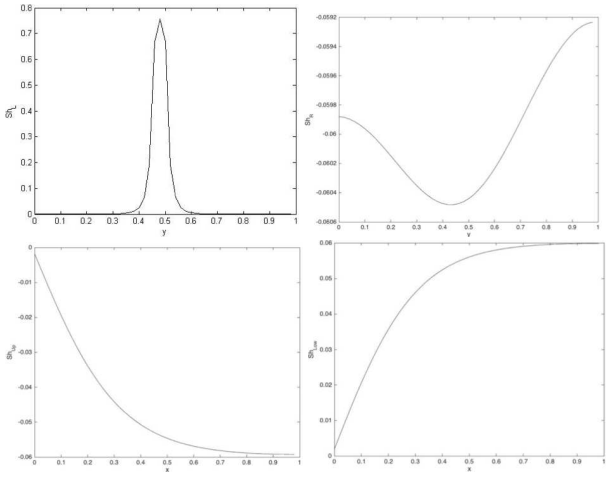

Fig. 11: Local Sherwood number distributions along the left wall, the right wall, the upper wall, and the lower wall, Case 2

5 Conclusions

In this paper, we have studied the simulations of non-isothermal single-phase flow in porous media. Using an adaptive multiscale time-stepping scheme. The proposed scheme is controlled by evaluating the CFL conditions, namely, $\mathrm{CFL}_{T,x}$, $\mathrm{CFL}_{T,y}$, $\mathrm{CFL}_{C,x}$ and $\mathrm{CFL}_{C,y}$ are calculated at each sup-step and checked if they are satisfied i.e. (CFL<1). We have used the CCFD method to discretize the governing equations. Some numerical experiments of the proposed scheme have been employed. Temperature, concentration, pressure, velocity, local Nusselt number and local Sherwood number, are shown in graphs. The local Nusselt number profiles along the left wall, right wall, upper wall, and lower wall of the square porous cavity have been investigated for the two cases of boundary conditions. The heat transfer rate in terms of the local Nusselt number has Gaussian-like distribution which is symmetric around the inlet location. Similar conclusions can be drawn for the mass-transfer rate behavior.

Acknowledgments

The first author is thankful to the Effat University Deanship of Graduate Studies and research for providing the financial support through internal research grants system, Decision No. UC#8/30.APR.2017/10.2-30(F).

References

[1] J. Bear, Dynamics of Fluid in Porous Media, Dover Publications, New York, (1968).

[2] K. Vafia, Hand Book of Porous Media, Marcel Dekkr, New York (2000).
[3] D. A. Nield and A. Bejan, Convection in Porous Media, Second Edition, Springer, New York (1999).
[4] N. H. Saeid and I. Pop., Viscous Dissipation Effect on Free Convection in Porous Cavity, Int. Comm. Hear Mass Tran., Vol. 31, pp. 723-732 (2004).
[5] M. A. Sheremet and I. Pop., Mixed Convection in a Lid-Driven Square Cavity Filled by a Nanofluid: Buongiorno's Mathematical Model, App. Math. Comp., Vol. 266, pp. 792-808 (2015).
[6] M. M. Ghalambaz, F. Sheremet, A. Mikhail and I. Pop., Triple-Diffusive Natural Convection in a Square Porous Cavity, Trans. Porous Media, Vol. 111, pp. 59-79 (2016).
[7] P. H. S. Carvalho and M. J. S. de Lemos, Passive Laminar Heat Transfer Across Porous Cavities Using Thermal Non-Model, Numer. Heat. Transfer, Vol. 66, pp. 1173-1194 (2014).
[8] A. C. Baytas and I. Pop, Free Convection in a Square Porous Cavity Using a Thermal Nonequilibrium Model. Int. J. Therm. Sc., Vol. 41, pp. 861-870 (2002).
[9] Z. Chen, G. Huan and Y. Ma, Computational Methods for Multiphase Flows in Porous Media , SIAM Comp. Sc. Eng. Philadelphia (2006).
[10] K. H. Coats, IMPES Stability: Selection of Stable Time Steps, SPE Reservoir Simulation Symposium, SPE 84924, Houston TX, February (2001).
[11] J. Lang and W. Hundsdorfer, Extrapolation-Based Implicit-Explicit Peer Methods with Optimised Stability Regions, J. Comp. Phys., Vol. 337, pp. 203-215 (2017).
[12] R. Burger, P. Mulet, L. Rubio and M. Sepulveda, Linearly Implicit-Explicit Schemes for the Equilibrium Dispersive Model of Chromatography, App. Math. Comp., Vol. 317, pp. 172-186 (2018).
[13] M. K. Kadalbajoo, A. Kumar and L. P. Tripathi, A Radial Basis Function Based Implicit-Explicit Method for Option Pricing under Jump-Diffusion Models, App. Num. Math., Vol. 110, pp. 159-173 (2016).
[14] A. Gravouil, A. Combescure. Multi-Time-Step Explicit-Implicit Method for Non-Linear Structural Dynamics, Int. J. Num. Meth. Eng., Vol. 50, pp. 199-225 (2000).
[15] S. M. Bhallamudi, S. Panday and P. S. Huyakorn. Sub-Timing in Fluid Flow and Transport Simulations, Adv. Water Res., Vol. 26, pp. 477-489 (2003).
[16] M. F. El-Amin, J. Kou, S. Sun and A. Salama. Adaptive Time-Splitting Scheme for Two-Phase Flow in Heterogeneous Porous Media. Adv. Geo-energ. Res., Vol. 1, pp. 182-189 (2017).
[17] T. Zhang and Y. Qian, The Time Viscosity-Spilling Method for the Boussinesq Problem, J. Math. Anal. App., Vol. 445, pp. 186-211 (2017).
[18] M. Caliari and S. Zuccher, Reliability of the Time-Splitting Fourier Method for Singular-Solutions in Quantum Fluids, Comp. Phys. Comm., Vol. 222, pp. 46-58 (2018).
[19] M. F. El-Amin, J. Kou and S. Sun, Discrete-Fracture-Model of Multi-Scale Time-Splitting Two-Phase Flow Including Nanoparticles Transport in Fractured Porous Media, J. Comp. App. Math., Vol. 333, pp. 327-349 (2018).
[20] M. F. El-Amin, J. Kou, A. Salama and S. Sun. An Iterative Implicit Scheme for Nanoparticles Transport with Two-Phase Flow in Porous Media. Proc. Comp. Sc., Vol. 80, pp. 1344-1353 (2016).
[21] M. F. El-Amin, J. Kou, A. Salama and S. Sun, Multiscale Adaptive Time-Splitting Technique for Nonisothermal Two-Phase Flow and Nanoparticles Transport in Heterogenous Porous Media, SPE-186047-MS, SPE Reservoir Characterisation and Simulation Conference and Exhibition, 8-10 May, Abu Dhabi, UAE (2017).
[22] M. F. El-Amin, Double Dispersion Effects on Natural Convection Heat and Mass Transfer in Non-Darcy Porous Medium, Appl. Math. Comp., Vol. 156, pp. 1-17 (2004).
[23] M. F. El-Amin, J. Kou and S. Sun, Convergence Analysis of the Nonlinear Iterative Method for Two-Phase Flow in Porous Media Associated with Nanoparticle Injection, Int. J. Num. Meth. Heat Fluid Flow, Vol. 27, pp. 2289-2317 (2017).
[24] M. Dehghan, Time-splitting Procedures for the Solution of the Two-Dimensional Transport Equation, Kybernetes, Vol. 36, pp. 791-805, (2007).
[25] D. Max, M. Massot, S. Descombes, C. Tenaud, T. Dumont, V. Louvet and F. Laurent. New Resolution sSrategy for Multiscale Reaction Waves Using Time Operator Splitting, Space Adaptive Multiresolution, and Dedicated High Order Implicit/Explicit Time Integrators, SIAM J. Sc. Comp., Vol. 34, pp. A76-A104 (2012).

Mohamed F. El-Amin is a Full Professor at Effat University, Jeddah, Saudi Arabia and a Visiting Professor at King Abdullah University of Science and Technology (KAUST) in Saudi Arabia, and he also was a Professor at Aswan University, Egypt. As a mathematician, he has over 23 years of research experience in the field of computational mechanics, applied mathematics, reservoir simulation, heat and mass transfer, fluid dynamics, transport phenomena, and turbulence. After obtaining his PhD in applied mathematics in 2001, he held research positions in several universities including South Valley University (Egypt), Stuttgart University (Germany), and Kyushu University (Japan). He is a fellow of Alexander von Humboldt (AvH), and JSPS. The research of Dr. El-Amin has resulted in around 140 journal and conference papers and book chapters; and three edited books. He is referee and guest editor of some specialized journals.

Shereen Abdel-Naeem is a graduate student at Mathematics Department, Faculty of Science, Aswan University. She received the BSc degree of Mathematics from South Valley University.

Nehma A. Ebrahiem is a Assistant Professor at at Mathematics Department, Faculty of Science, Aswan University. She received the PhD degree of Mathematics from South Valley University at 2003.